Deformation behavior of typical inclusions in GCr15 during hot rolling process

Y.-H. Jiang [a], Q.-Q. Mou [b], X.-D.Deng [a], R.A. Muvunyi [a], J.-L. Li [a,c, *]

[a] Hubei Provincial Key Laboratory for New Processes of Ironmaking and Steelmaking, Wuhan University of Science and Technology, Wuhan, 430081, China
[b] CNCEC-EEC Dajiang Environmental Protection Technology Co., LTD., Huangshi 435000, Hubei, China
[c] Key Laboratory for Ferrous Metallurgy and Resources Utilization of Ministry of Education, Wuhan University of Science and Technology, Wuhan, 430081, China
* Corresponding author: Jianli Li, jli@wust.edu.cn

(Received 05 September 2024; Accepted 10 December 2024)

Abstract

Non-metallic inclusions significantly impact the lifespan of bearing steel. Investigating the deformation behavior of these inclusions during the rolling process is crucial for controlling their shape and size in production. This study focuses on GCr15 bearing steel, a representative grade of bearing steel, and utilizes the finite element software ABAQUS to simulate the deformation of Al_2O_3 inclusions, MnS inclusions, and Al_2O_3-MnS composite inclusions after hot rolling of GCr15 steel. The findings indicate that when the size of inclusions is within 10 μm, their type and shape have a more significant impact than variations in size. Among them, Al_2O_3-MnS composite inclusions exhibit the least harm to the steel matrix. The stress concentration of Al_2O_3 inclusions will appear on the MnS cladding layer, which can slow down the occurrence of cracks. Additionally, the aspect ratio of MnS inclusions decreases after rolling, diminishing its influence on the steel matrix's anisotropy. Simultaneously, composite inclusions can harmonize the deformation capabilities of the inclusions and the steel matrix, thereby minimizing the likelihood of void formation. Consequently, in the smelting process, it is beneficial to modify inclusions into regular circular shapes and form composite Al_2O_3-MnS inclusions to mitigate their detrimental effects on the steel matrix.

Key words: *Hot rolling; Complex inclusions; Stress concentration; Strain difference; Finite element simulation*

1. Introduction

With the industrialization of various societal sectors, the use of bearing steel has become increasingly widespread. This type of steel is commonly utilized in high-end equipment fields such as aerospace, transportation, mining machinery, and marine engineering due to its ability to withstand harsh working environments. Consequently, it demands high fatigue strength and impact toughness in high-speed and heavy-load conditions [1-3]. The performance of bearing steel is contingent upon its material composition, forging or rolling processes, and heat treatment methods. In light of

environmental protection and energy conservation imperatives, there is a pressing need to enhance the quality of bearing steel to sustain higher loads without enlarging its size or weight. Inclusion in bearing steel is one of the main factors affecting its life. Therefore, it is very important to study the deformation behavior of inclusions in steel to clarify the harm of inclusions [4,5].

The presence of inclusions in steel can lead to stress concentration when subjected to alternating loads, thereby disrupting the continuity of the steel matrix [6,7]. Different types of inclusions possess varying degrees of hardness, brittleness, and thermal expansion coefficients, which means that the severity of defects they induce also varies. Brittle inclusions, such as Al_2O_3 and TiN, are particularly prone to causing stress concentrations during processing, which may result in cracks forming within the steel matrix [8-11]. The influence of the plastic inclusion MnS on the fatigue properties of bearing steel is a subject of debate. Some scholars believe that the fatigue of steel is mainly related to the size of inclusions. MnS will promote the nucleation of voids during deformation, which can easily lead to quasi-cleavage fracture and failure of materials [12,13]. Conversely, other research posits that plastic inclusions can encapsulate brittle inclusions, thereby mitigating the stress around them. This mechanism allows for a more harmonious deformation between the inclusions and the matrix, ultimately diminishing the detrimental effects associated with brittle inclusions [13,14].

Currently, research on the deformation of inclusions during the rolling process primarily relies on field data and finite element simulations, with experimental studies playing a supplementary role. Compared to experimental studies, finite element simulations are more cost-effective and time-efficient, allowing for a more intuitive observation of the entire inclusion deformation process. Matsuika [15] selected Al_2O_3 and MnS as representative inclusions in a steel matrix and utilized DEFORM-2D to simulate a uniaxial compression experiment. The relationship between the flow stress ratio of inclusions to the steel matrix and the aspect ratio of inclusions post-compression was examined by comparing the results with those from the uniaxial compression experiment. Gupta [16] employed ANSYS-2D software to simulate the stress and strain experienced by inclusions of varying hardness during hot rolling at temperatures ranging from 800°C to 1400°C, utilizing both macro and micro models. The findings indicated that inclusions with higher hardness are more prone to generating voids at the interface between the steel matrix and the inclusions. Wang [17] chose MnO, Al_2O_3, and SiO_2 composite inclusions and used ABAQUS-3D software to simulate the deformation of these composite inclusions under different temperatures, reductions, and steel grades, unveiling the mechanism behind void formation between inclusions and the steel matrix. Zhang [18] applied ANSYS, selecting Al_2O_3 and MnS as typical inclusions in the steel matrix, and employed a thickness reduction transfer method to simulate crack propagation around the inclusions. Ge [19] utilized ABAQUS-2D to simulate the formation of voids around Al_2O_3 inclusions during CSP hot rolling through a 'deformation accumulation' approach. Guo [20] used ABAQUS-2D to simulate the deformation of Al_2O_3, MnS, AlN, and TiN inclusions, as well as AlN-MnS and Al_2O_3-AlN composite inclusions during compression. The study revealed that inclusions with

lesser deformation capabilities generate greater stress within the steel matrix. In the above rolling simulation, the size of the inclusions ranges from 50 to 1000 μm. However, in actual production, the inclusions are smaller and have a larger size ratio relative to the matrix. Most studies focus on the rolling deformation of single inclusions, with few investigations into composite inclusions.

In this study, a rudimentary rolling model was constructed using ABAQUS-2D. Al_2O_3 and MnS inclusions, as well as Al_2O_3-MnS composite inclusions with varying hardness, were selected as typical inclusions in the steel matrix. The deformation of these inclusions, ranging in size from 2 to 20 μm and differing in shape and hardness, during the hot rolling of steel was simulated. The impact of these inclusions on the steel matrix was evaluated by analyzing the stress and strain exerted on both the inclusions and the steel matrix.

2. Establishment of the model

2.1. Mathematical model

During the rolling process, the deformation of the rolled piece undergoes an uneven deformation process. Concurrently, various regions of the rolled piece may experience plastic deformation, an elastic state, or a transitional stage from an elastic state to plastic deformation. In such cases, the Prandtl-Reuss theory of plastic flow separates the strain rate into elastic and inelastic components [21,22]:

$$d\varepsilon_{ij} = d\varepsilon_{ij}^{e} + d\varepsilon_{ij}^{p} \tag{1}$$

where $d\varepsilon_{ij}$ is total strain increment; $d\varepsilon_{ij}^{e}$ is elastic strain increment; $d\varepsilon_{ij}^{p}$ is increment of plastic strain. According to the generalized Hooke 's law, the elastic strain increment is:

$$d\varepsilon_{ij}^{e} = \frac{1-2\nu}{3E}\delta_{ij}d\sigma_{kk} + \frac{1+\nu}{E}dS_{ij} \tag{2}$$

where $d\varepsilon_{ij}^{e}$ is elastic strain increment; σ_{kk} is mean stress; E is elastic modulus; ν is poisson ratio; S_{ij} is deviator stress tensor; According to the Levi-Mises increment theory, the plastic strain increment is:

$$d\varepsilon_{ij}^{p} = \alpha dS_{ij} \tag{3}$$

where $d\varepsilon_{ij}^{p}$ is increment of plastic strain; S_{ij} is deviator stress tensor; α is the scaling factor, $\alpha = 1$ is the plastic state, $\alpha = 0$ is the elastic state. The constitutive equation of elastic-plastic material can be obtained by combining Eq. (1), Eq. (2) and Eq. (3):

$$d\varepsilon_{ij} = \frac{1-2\nu}{3E}\delta_{ij}d\sigma_{kk} + \frac{1+\nu}{E}dS_{ij} + \alpha dS_{ij} \tag{4}$$

In the hot working process of metals, the deformation resistance is related to temperature, strain and strain rate [19]. Pan [24] carried out the hot compression test of GCr15 bearing steel on the Gleeb-3500 thermal simulation machine, and obtained the flow stress constitutive equation of GCr15 bearing steel at high temperature:

$$\sigma = \frac{1}{\alpha} ln\{\left[\frac{\dot{\varepsilon} exp(Q/RT)}{A}\right]^{1/n} + \left[\left(\frac{\dot{\varepsilon} exp(Q/RT)}{A}\right)^{2/n} + 1\right]^{1/2}\} \tag{5}$$

where σ is high temperature flow stress; α is stress level constant; $\dot{\varepsilon}$ is strain rate; Q is hot deformation activation energy; R is gas constant, 8.314 $J \cdot mol^{-1} \cdot K^{-1}$; T is thermodynamic temperature; , A, n is temperature-dependent material constants.

2.2. Geometric model of inclusions

According to the results of references [30-32], the inclusions in GCr15 steel primarily exist as Al_2O_3, MnS, and Al_2O_3-MnS composite inclusions. Considering the typical morphology of these inclusions, Al_2O_3 inclusions are represented by square and circular shapes, MnS inclusions by circular and elliptical shapes with an aspect ratio of 2, and Al_2O_3-MnS composite inclusions by circular MnS encapsulating circular Al_2O_3 and square Al_2O_3 shapes. The two-dimensional geometric model of these inclusions is illustrated in Fig. 1.

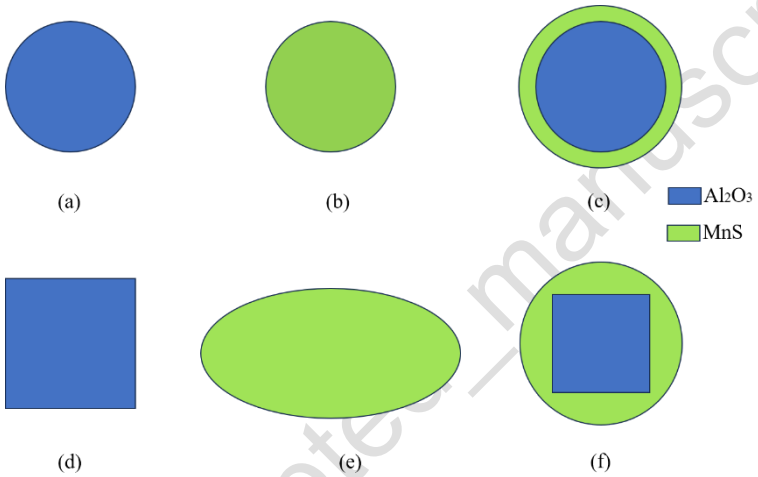

Fig. 1. *Two-dimensional model of different inclusions:(a) circular Al_2O_3;(b) Circular MnS; (c) Circular Al_2O_3-MnS; (d) Square Al_2O_3; (e) Elliptic MnS; (f) Circular Al_2O_3-MnS*

There are significant size differences in the inclusions found in steel materials. In this study, the size of these inclusions is considered a variable in our simulations. We observed an increase in the side length of square Al_2O_3 inclusions and the diameter of circular Al_2O_3 inclusions, ranging from 2 μm to 10 μm. Similarly, the diameter of circular MnS inclusions and the short axis length of elliptical MnS inclusions also expanded from 2 μm to 10 μm. In the Al_2O_3-MnS composite inclusion, the diameter of the outer MnS inclusion layer escalated from 5 μm to 10 μm, while the side length of the inner square Al_2O_3 inclusion was 3 μm, and the diameter of the circular Al_2O_3 inclusion was 4 μm. The size of the inner brittle inclusion remained constant throughout. This research exclusively examined the impact of MnS inclusions with varying thicknesses on the outer layer of brittle inclusions.

2.3. Related physical parameters

The rolling model parameters of the hot rolling process are shown in Table 1. The length of the rolled piece is 200 mm, the width is 100 mm, and the inclusion position is set at the center of the rolled piece. The start rolling temperature of hot rolling is 1100℃, and the chemical composition of GCr15 steel is shown in table 2. According to reference [24], α、$\dot{\varepsilon}$、Q、A、n the values of and n are 0.00971, 325270, 325.27, 3.018×10^{12} and 4.573, respectively. The flow stress of GCr15 steel is calculated by Eq.

(5), and the results are shown in Table 3.

The physical parameters of Al_2O_3 inclusions at high temperature are difficult to obtain. In this paper, the parameters of high temperature Al_2O_3 ceramics at 1100 ℃ are used [19,25]. The physical parameters of MnS inclusions at 1100 ℃ refer to Jin 's literature [19,26], and other parameters are shown in Table 4.

Table 1. *Rolling parameters*

Roll diameter(mm)	150
Rolling speed (mm/sec)	942
Slab length L(mm)	200
Slab width H(mm)	100
Inclusion position	(1/2 L, 1/2H)
Inclusion shape	Circle, Ellipse, Square
Rolling temperature (℃)	1100
Reduction(mm）	10
Degree of reduction (%)	10

Table 2. *Chemical composition of GCr15 bearing steel*

Element	**Fe**	**C**	**Si**	**Mn**	**Cr**
Content /*wt.*%	Margin	0.95~1.05	0.40~0.65	0.90~1.20	1.35~1.65
Element	**P**	**S**	**Cu**	**Ni**	**Cu+Ni**
Content /*wt.*%	≤0.027	≤0.020	≤0.25	≤0.30	≤0.50

Table 3. *Flow stress (ε=1 s^{-1})*

Temperature (℃)	950	1000	1050	1100
Flow stress (MPa)				
GCr15	150.3	125.7	104.6	86.9
Al_2O_3	300	250	200	160
MnS	50	45	38	28

Table 4. *Physical parameters*

	GCr15	Al_2O_3	MnS
Density /g· cm^{-3}	7.810	3.95	4.057
Young's modulus /MPa	1.96×10^{11}	3×10^{11}	1.38×10^{11}

Poisson ratio	0.3	0.3	0.3

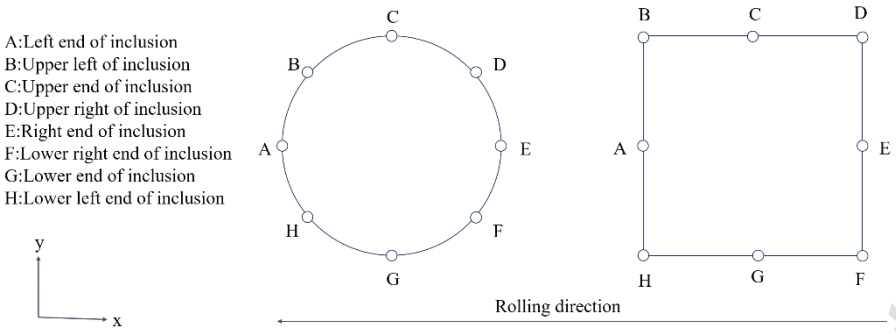

Fig. 2. *Two-dimensional schematic diagram of inclusions*

The deformation behavior of inclusions in steel in the field experiment, the problem of large difference between the size of slab and inclusion will be encountered. Controlling the composition of micron-sized inclusions in advance and incorporating them into a slab during field experiments presents significant challenges. While numerical simulation offers a viable solution, it is not without its pitfalls, as inclusions are susceptible to mesh distortion during the computational process. To address these multi-scale challenges and mitigate mesh distortion, several techniques have been explored, including transitional mesh segmentation, thickness reduction transfer, and the submodel approach [18,19,23]. In this research, we opt for the submodel technique. This involves extracting specific areas from the global model and subsequently implanting spherical inclusions within these regions to formulate a matrix submodel that encapsulates the inclusions. This strategy facilitates a localized refinement of the mesh surrounding the inclusion without necessitating an overwhelming increase in computational demand. As depicted in Fig. 3, both the primary model and the submodel utilize the CPE4RT grid type. Following the meshing of the primary model, the steel matrix comprises a total of 20,000 elements. Upon refinement of the submodel, there are 2,628 elements present, and each 2 μm circular inclusion is represented by 96 elements.

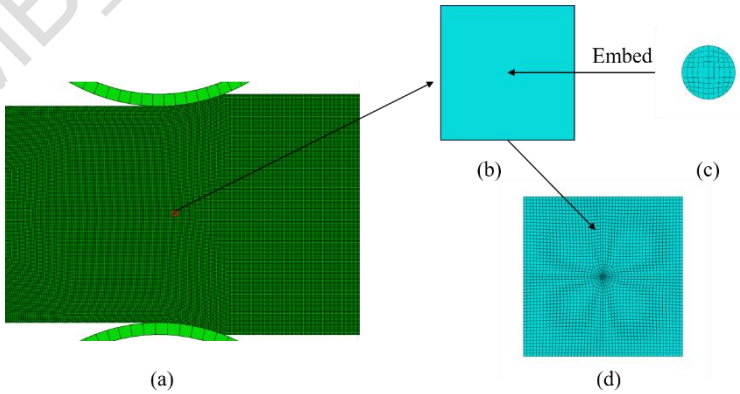

Fig. 3. *Submodel method: (a) Rolling model; (b) Splitting the grid; (c) Inclusions; (d) Submodel*

In an effort to streamline the model, certain conditions that exert minimal influence on the hot rolling process are idealized. Furthermore, the following assumptions are introduced for the developed model:

(1) The roll in the model is rigid, while the rolled piece and its inclusions consist of elastic-plastic materials;

(2) The properties of the rolled piece and its inclusions exhibit isotropy;

(3) Cohesion between the rolled piece and the inclusion is not accounted for;

(4) The friction coefficient between the roll and the rolled piece remains constant at 0.3, and the rolled piece and the inclusion are perfectly integrated, disregarding friction between the steel matrix and the inclusion;

(5) The temperature of the rolled piece is maintained throughout the rolling process, ensuring uniform temperature across all positions of the rolled piece;

(6) No residual stress is present at the inclusion, and the propensity for cavity formation and cracking is assessed through stress field analysis and strain differences, without delving into fracture mechanics.

3. Results

3.1. Effect of MnS inclusions on steel matrix

The plasticity of MnS inclusions varies under different temperature conditions. In this study, a hot rolling temperature of 1100 °C was chosen, as it results in the highest relative plasticity of MnS inclusions [27,28]. This increased plasticity allows for a more pronounced difference between MnS and Al_2O_3 inclusions, enabling better observation of the changes in various plastic inclusions within the steel matrix. As illustrated in Fig. 4, whether the inclusion is a regular circle or an elliptical MnS inclusion with a length-width ratio of 2, the maximum strain shifts from the positive center of the inclusion to the BDFH of the inclusion. However, the strain at both the center and the BDFH of the inclusion gradually decreases. This phenomenon can be attributed to the diminishing influence of longitudinal and transverse stresses of the same size on the inclusion's strain as its size increases. From the results, it is evident that smaller MnS inclusions are more likely to deform into slender strip MnS inclusions during rolling.

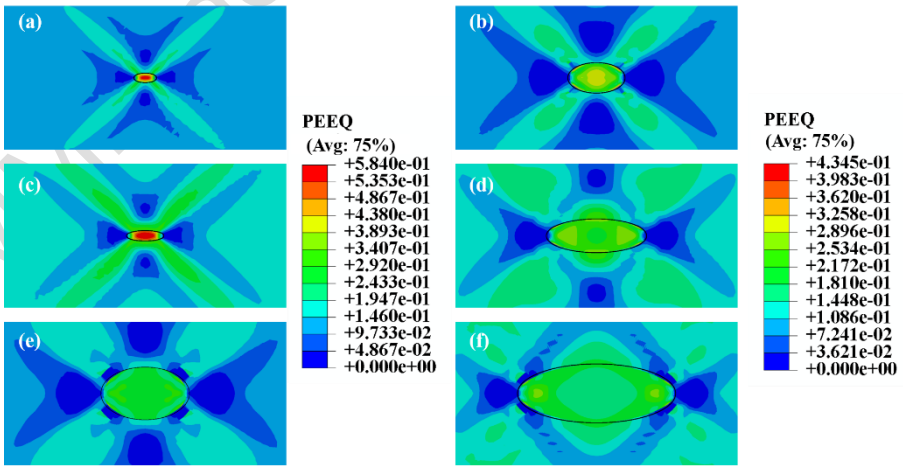

Fig. 4. *Strain distribution of circular and elliptical MnS inclusions with different sizes*
Diameter of round MnS: (a) 2 μm; (c) 6 μm; (e) 10 μm;
Elliptical MnS minor axis length: (b) 2 μm; (d) 6 μm; (f)10 μm

3.2. Effect of Al_2O_3 inclusions on steel matrix

The variation in size of idealized circular Al_2O_3 inclusions influences stress distribution. As illustrated in Fig. 5, the stress at point AE for these circular inclusions diminishes with increasing size, whereas the peak stress consistently occurs at BDFH. In contrast, the stress distribution for square Al_2O_3 inclusions remains unaffected by size changes. The peak stress values for both square and circular Al_2O_3 inclusions are observed at BDFH, but the magnitude for square inclusions exceeds that of circular ones. Notably, as the size increases, there is minimal alteration in the peak stress for either type of inclusion. The peak stress for circular Al_2O_3 inclusions consistently approximates 160 MPa, while for square Al_2O_3 inclusions, it consistently approximates 450 MPa. This suggests that, relative to size, the shape of the inclusion exerts a more pronounced impact on stress, with the size effect primarily influencing the area subjected to peak stress.

Fig. 6 illustrates the strain on the steel matrix surrounding Al_2O_3 inclusions. Circular Al_2O_3 inclusions remain undeformed post-rolling, whereas square Al_2O_3 inclusions exhibit minor deformation at their four corners. The strain distribution around various shapes of Al_2O_3 inclusions remains consistent, irrespective of size. The strain and stress are concentrated at the four corners of the square Al_2O_3 inclusions. The peak stress for square Al_2O_3 inclusions coincides with the location of strain, while circular Al_2O_3 inclusions, being more uniform, experience less stress and no deformation. Observing the strain around the Al_2O_3 inclusions, it can be seen that the strain distribution of Al_2O_3 inclusions with different shapes is the same after rolling. The maximum strain around the inclusion is at ACEG, and the strain near the inclusion is 0. Therefore, between the inclusions and the steel matrix, the ACEG is the place with the largest strain difference. Due to the generation of strain difference, the steel matrix and the inclusions will have a force that separates the two due to deformation, and the larger the strain difference, the greater the force generated. When the force generated is greater than the bonding force between the inclusions and the steel matrix, the two will be separated to produce voids. This phenomenon will subsequently evolve into cracks, which is extremely harmful to the performance of steel. After calculation, the strain difference generated at A is the largest, because the AE is along the rolling direction, and the lateral deformation will be greater than the longitudinal deformation. Due to the inertia generated by the movement of the rolled piece during the rolling process, the inclusions will move slightly backward, which also leads to the phenomenon that the strain at A is slightly larger than that at E. All in all, the probability of voids at A is greater.

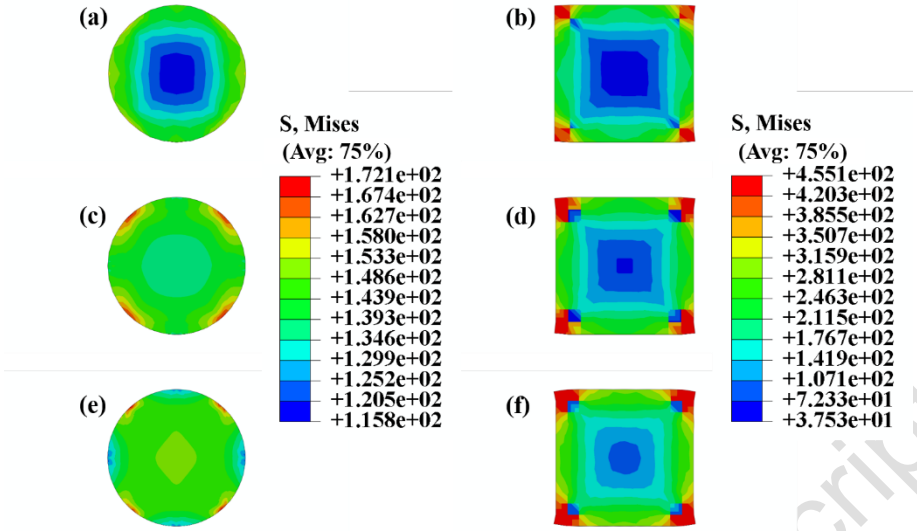

Fig. 5. *The stress distribution of Al_2O_3 inclusions with different sizes and shapes: Circular diameter: (a) 2 μm; (b) 6 μm; (c) 10 μm; Square side length: (d) 2 μm; (e) 6 μm; (f) 10 μm*

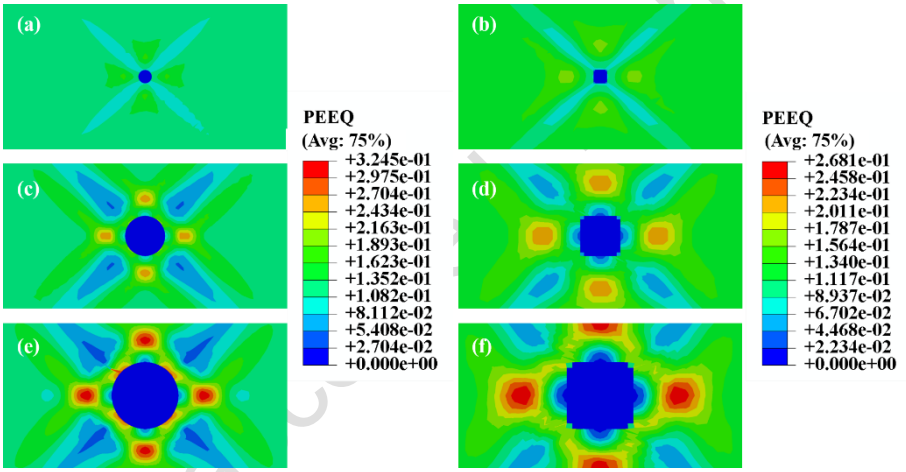

Fig. 6. *Strain distribution of Al_2O_3 inclusions with different sizes: Circular diameter: (a) 2 μm; (b) 6 μm; (c) 10 μm; Square side length: (d) 2 μm; (e) 6 μm; (f) 10 μm*

3.3. Effect of Al_2O_3-MnS composite inclusions on steel matrix

For Al_2O_3-MnS composite inclusions, the diameter of MnS inclusions was set to gradually increase from 5μm to 10μm, and spherical Al_2O_3 inclusions with a diameter of 4μm and square Al_2O_3 inclusions with a side length of 3μm were embedded in them, respectively. The difference in size between the two is to control the volume gap between the two and reduce the error.As depicted in Fig. 7, the MnS inclusion layer does not alter the stress distribution of the intermediate Al_2O_3 inclusion, and the maximum stress distribution of the Al_2O_3 inclusion remains at BDFH. However, the stress of Al_2O_3 inclusions with different shapes diminishes as the thickness of the MnS inclusion coating layer increases, thereby reducing the likelihood of stress concentration and crack initiation in Al_2O_3 inclusions. Concurrently, since the maximum stress of the square Al_2O_3 inclusion is at the MnS inclusion, this facilitates the transfer of crack initiation from the steel matrix to the inclusion, which is

advantageous for the steel matrix.

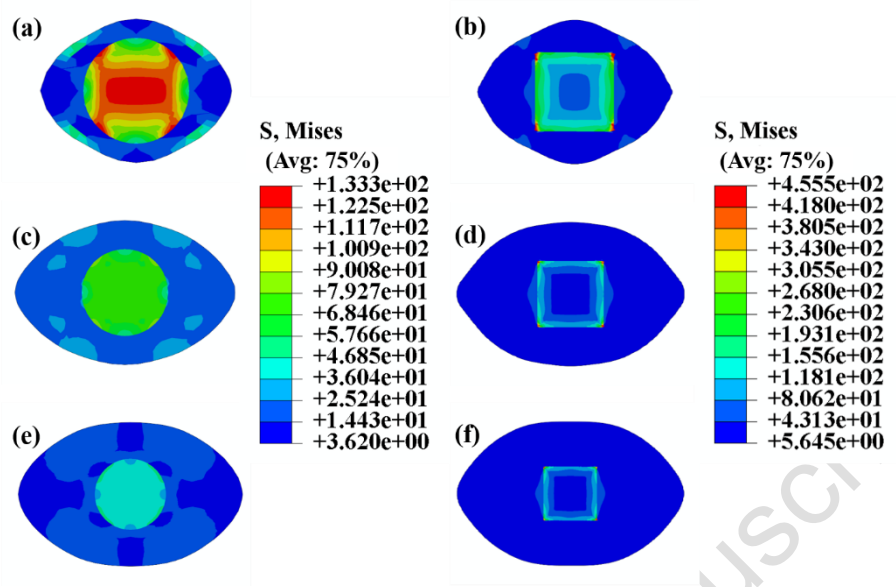

Fig. 7. *Stress distribution of Al_2O_3-MnS inclusions with different sizes and shapes*
Composite inclusion size: round Al_2O_3: (a) 6 μm; (b) 8 μm; (c) 10 μm;
Square Al_2O_3: (d) 6 μm; (e) 8 μm; (f) 10 μm

As illustrated in Fig. 8, the application of a MnS inclusion coating results in a diminished strain within the steel matrix, as well as a reduced strain difference between the inclusion and the matrix. This observation confirms that MnS inclusions can effectively mediate the deformation between inclusions and the steel matrix, thereby mitigating crack formation induced by voids surrounding the inclusions. Notably, the deformation capacity of MnS inclusions is curtailed, and their deformation remains subdued compared to isolated MnS inclusions of equivalent size following rolling. Such an effect diminishes the impact of MnS inclusions on the steel matrix's anisotropy.

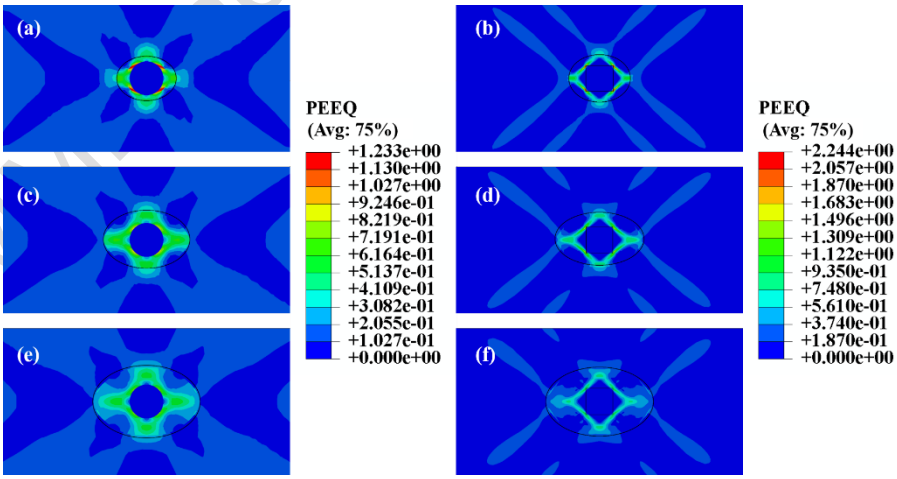

Fig. 8. *Strain distribution of Al_2O_3-MnS composite inclusions with different sizes*
Composite inclusion size: round Al_2O_3:
(a) 6 μm; (b) 8 μm; (c) 10 μm; Square Al_2O_3: (d) 6 μm; (e) 8 μm; (f) 10 μm

As illustrated in Fig. 9, a comparative analysis of the stress distribution for Al_2O_3 inclusions, MnS inclusions, and Al_2O_3-MnS composite inclusions of identical size but

varying shapes within the steel matrix reveals that the stress distribution patterns and maximum stress values for identical inclusions are similar. The difference between different kinds of inclusions is that the matrix with MnS inclusions is less stressed where the strain is small. Although the degree of stress reduction is obvious, the area where the stress can be reduced is small. In general, it has little effect on the rolled piece.These findings indicate that while inclusions influence the stress magnitude and distribution in the steel matrix, the impact of different inclusion types and shapes is relatively consistent.

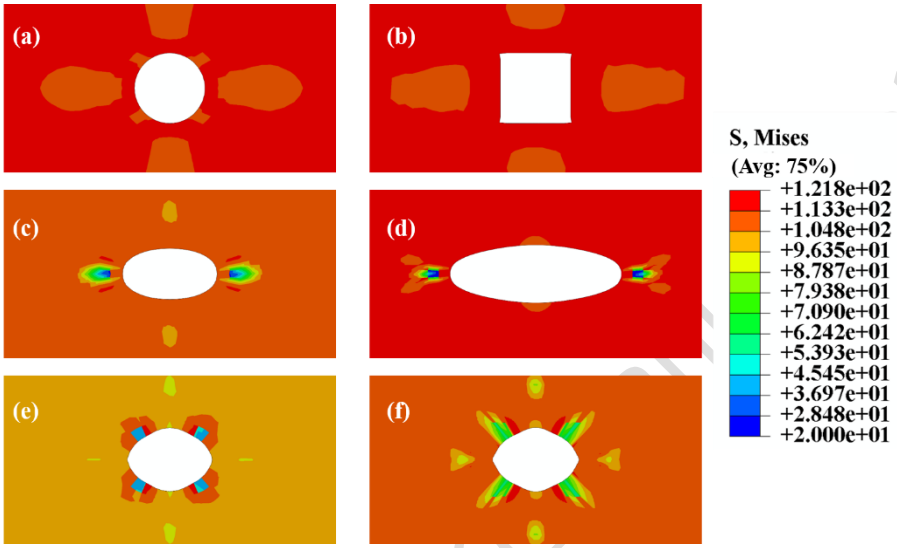

Fig. 9. *The stress distribution of different kinds of 6 μm inclusions: (a)circular Al_2O_3; (b) Square Al_2O_3; (c) Circular MnS; (d) Elliptic MnS; (e) Circular Al_2O_3 in circular Al_2O_3-MnS; (f) Square Al_2O_3 in circular Al_2O_3-MnS*

4 Discussion

As demonstrated in Fig. 10, a statistical analysis was conducted on the length-width ratios of circular and elliptical MnS inclusions of varying sizes after rolling. It is evident that the length-width ratio of elliptical MnS inclusions diminishes as their size increases, surpassing that of standard circular MnS inclusions. Smaller elliptical MnS inclusions are more susceptible to deformation, resulting in a larger aspect ratio post-rolling. This increased aspect ratio can potentially lead to disparities in the horizontal and vertical performance of steel, thereby adversely affecting its properties.

Fig. 11 displays the maximum stress statistics for circular and square Al_2O_3 inclusions of varying sizes. For circular Al_2O_3 inclusions, an increase in size corresponds to a rise in maximum stress, albeit the change is subtle. Conversely, the maximum stress experienced by square Al_2O_3 inclusions remains largely unchanged with increasing size. This stability can be attributed to the stress concentration primarily occurring at the tips of the square inclusions, unaffected by size variations. In manufacturing processes, mitigating the presence of square or sharply shaped inclusions within Al_2O_3 can effectively reduce stress concentration phenomena.

As shown in Fig.6, after the rolling of Al_2O_3 inclusions with different shapes, the strain distribution of the steel matrix is similar. The strain between the steel matrix and the inclusions is different, and the strain of the steel matrix is greater than the strain of the inclusions. The strain difference will separate the inclusions from the steel matrix.

The larger the strain difference, the greater the force generated, and the easier it is to produce voids [29]. As illustrated in Fig. 12, an increase in size corresponds with a gradual rise in strain difference. Notably, circular Al_2O_3 inclusions exhibit a larger strain difference compared to square Al_2O_3 inclusions of equivalent size. Consequently, larger circular Al_2O_3 inclusions are more susceptible to void formation. This suggests that larger square Al_2O_3 inclusions pose a greater threat to the steel matrix integrity. To mitigate this risk, it is crucial to reduce their size and modify their shape to circular during the smelting process.

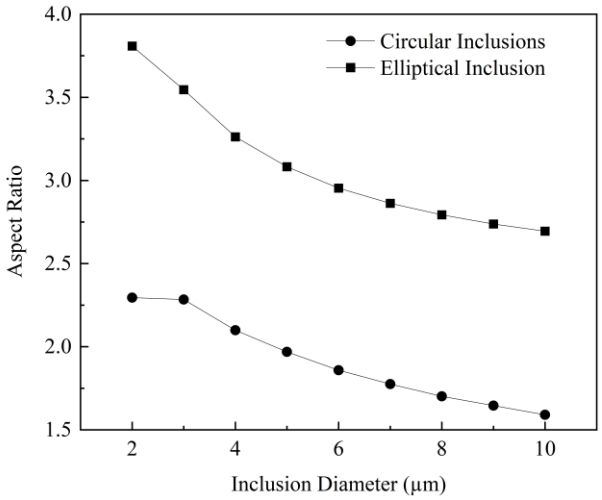

Fig. 10. *Aspect ratio of MnS inclusions with different sizes and shapes after rolling*

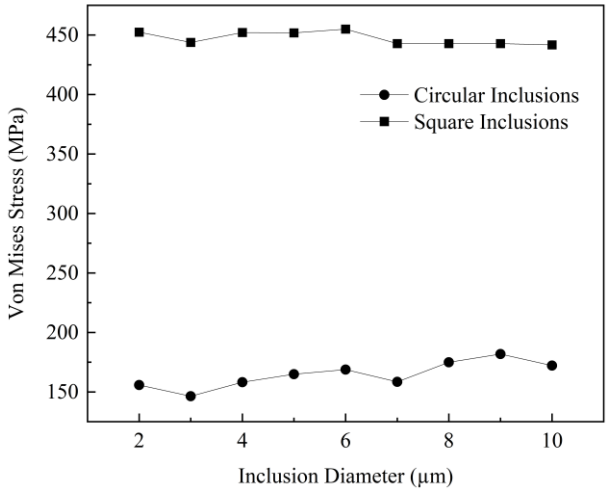

Fig. 11. *Maximum stress of Al_2O_3 inclusions with different sizes and shapes*

The stress of Al_2O_3-MnS composite inclusions of varying sizes was analyzed to derive Fig. 13. The results indicated that the peak stress of circular Al_2O_3 inclusions diminished progressively as the thickness of the MnS coating layer increased. In contrast, the stress in square Al_2O_3 inclusions remained unaffected by the MnS coating layer, consistently measuring approximately 450 MPa. For standard circular Al_2O_3 inclusions, the MnS coating effectively mitigated the stress concentration induced by

differing hardness values. However, for Al_2O_3 inclusions with tips, the MnS coating merely shifted the location of stress concentration without reducing its magnitude.

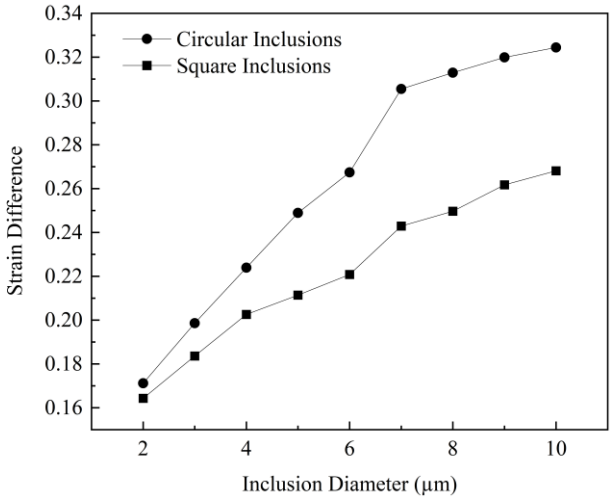

Fig. 12. *Strain difference at different positions of Al_2O_3 inclusions with different sizes and shapes*

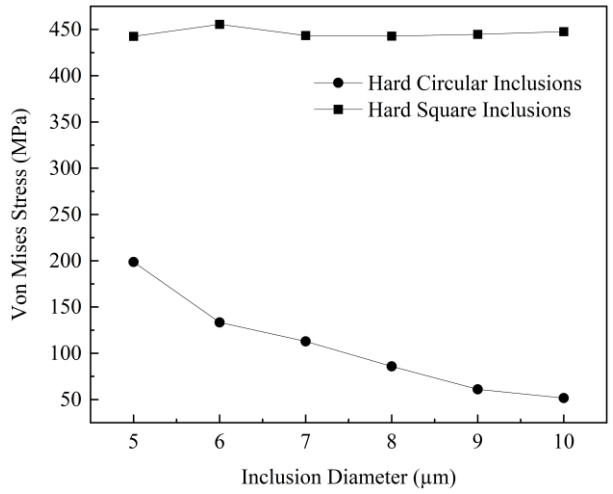

Fig. 13. *Maximum stress of Al_2O_3-MnS composite inclusions with different sizes after rolling*

The length-width ratio of Al_2O_3-MnS composite inclusions post-rolling is statistically depicted in Fig. 14. The Fig. illustrates that as the size of these inclusions increases, there is a corresponding increase in their length-width ratio. However, this ratio remains significantly smaller than that of a singular MnS inclusion after rolling. When compared to single plastic inclusions of equivalent size, composite inclusions exert a lesser influence on the steel matrix's anisotropy. Circular Al_2O_3 inclusions are more effective in inhibiting the deformation capability of MnS inclusions than their square counterparts. Consequently, even with a thin MnS coating, the stress on Al_2O_3 inclusions remains significant due to the excessive deformation of MnS inclusions. Conversely, when the MnS cladding layer is thick, the aspect ratio of the composite inclusions post-rolling is elevated, which can impact the steel matrix's anisotropy. This phenomenon is opposite to the change of single MnS inclusion with size. Although the

deformation of both inclusions is mainly MnS inclusions during rolling, there are Al_2O_3 inclusions in the composite inclusions to hinder the deformation of MnS inclusions. Observing a single MnS inclusion, it can be found that the maximum strain of the MnS inclusion is at the core during large deformation, but the core of the composite inclusion is an undeformed Al_2O_3 inclusion, which will make the deformation of the MnS inclusion shift from the core to the area around the core, and the aspect ratio of the inclusion after rolling becomes larger. However, as the size of MnS inclusions increases, the influence of Al_2O_3 inclusions will gradually decrease. The aspect ratio of composite inclusions reaches the maximum at 9μm, and then gradually returns to the deformation law of single MnS inclusions. With the increase of inclusion size, the aspect ratio after rolling decreases gradually.

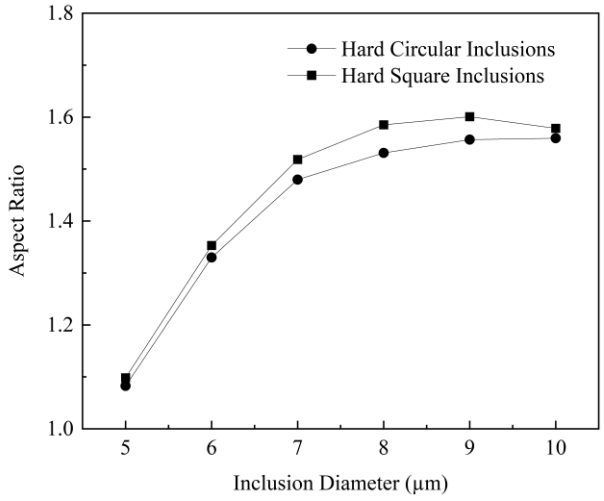

Fig. 14. *Aspect ratio of Al_2O_3-MnS composite inclusions with different sizes after rolling*

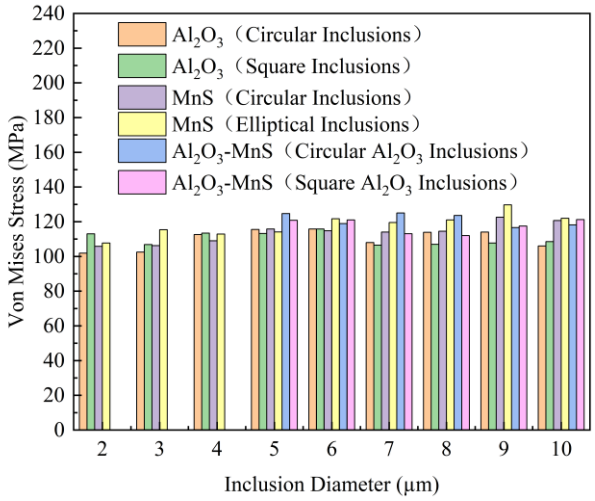

Fig. 15. The maximum stress of steel matrix around different inclusions with different sizes

Upon analyzing the maximum stress on the steel matrix, the results are depicted in Fig. 15. Observations from the Fig. indicate that the morphology and dimensions of the inclusions exert minimal influence on the peak stress experienced by the steel matrix.

The peak stress observed around the six distinct inclusions ranges between 100-120 MPa. Notably, the form of the inclusions predominantly impacts the stress distribution across the steel matrix. Among the evaluated inclusions, those composed of Al_2O_3 present the most critical stress distribution, characterized by the largest area of peak stress. Furthermore, the stress concentration surrounding the square Al_2O_3 inclusions is particularly pronounced, posing a heightened risk to the integrity of the steel matrix.

Currently, most studies on the size change of inclusions in steel are primarily related to rare earth elements. Rare earth treatment modifies these inclusions, making them rounder and promoting the formation of composite Al_2O_3-MnS inclusions, where MnS tends to wrap around Al_2O_3. Research indicates that as the size of these composite inclusions increases, their aspect ratio decreases after rolling [33]. Luo [34] found that the impact performance of steel plates treated with rare earth improves post-rolling. This improvement is attributed to reduced stress concentration in Al_2O_3-MnS composite inclusions compared to single Al_2O_3 inclusions, and a smaller aspect ratio compared to single MnS inclusions, resulting in lower probabilities of crack formation and reduced anisotropic effects. According to Wang's theory[35], rare earth treatment decreases the size of Al_2O_3 inclusions and transforms their shapes from elongated strips and sharp corners to more spherical forms, which can effectively enhance the performance of the rolled material. In summary, these experimental findings align well with the simulation results presented in this paper.

5 Conclusion

Through ABAQUS software, the deformation of MnS inclusions, Al_2O_3 inclusions and Al_2O_3-MnS composite inclusions with different sizes under the same reduction was simulated by submodel method. The effects of different sizes and different types of inclusions in GCr15 steel after rolling were investigated, and the harm of inclusions was evaluated:

(1) When the inclusion size is 2-10 μm, the stress distribution on the inclusion and the stress distribution and stress magnitude of the steel matrix around the inclusion change little with the change of the size of the three inclusions. At this time, the size of the inclusion has little effect on the inclusion for the steel matrix.

(2) When the size of inclusions is less than 10 μm, the more regular the shape of Al_2O_3 and MnS inclusions is, the closer they are to the circle, and the smaller the influence of the inclusions on the steel matrix is. The square Al_2O_3 inclusions cause larger strain and are more prone to cracks. The aspect ratio of elliptical MnS inclusions after rolling changes more, which is more likely to affect the anisotropy of steel.

(3) The effect of Al_2O_3-MnS composite inclusions on the properties of steel is smaller than that of single Al_2O_3 and MnS inclusions. The composite inclusions can not only eliminate the stress concentration of Al_2O_3 inclusions, but also reduce the realization ability of MnS inclusions. At the same time, it can also coordinate the strain difference between inclusions and steel matrix, so that the gap between the two is not easy to appear.

Acknowledgments

This work was financially supported by the National Natural Science Foundation o f China (No.52274341, 52404350), Central Government Guided Local Science and Te chnology Development Fund of Hubei Province (2023EGA040), and the State Key La boratory of Refractories and Metallurgy,Wuhan Uni-versity of Science and Technolog y.

Funding

This work was financially supported by the National Natural Science Foundatio n of China (No.52274341, 52404350), and Central Government Guided Local Scienc e and Technology Development Fund of Hubei Province (2023EGA040).

Conflicts of interest

The authors declare that they have no conflict of interest.

Data availability statement

The data generated and analyzed during the current study are not publicly availab le due to proprietary information but are available from the corresponding author on re asonable request.

Author contribution statement

Conceptualization, Yuhang Jiang and Xiaodong Deng; Methodology, Yuhang Jian g; Software, Xiaodong Deng; Validation, Yuhang Jiang, Xiaodong Deng and Qiqian g Mou; Formal Analysis, Yuhang Jiang; Investigation, RodrigueArmel Muvunyi; Reso urces, Jianli Li; Data Curation, Yuhang Jiang; Writing – Original Draft Preparation, Yu hang Jiang; Writing – Review & Editing, Jianli Li; Visualization, RodrigueArmel Muv unyi; Supervision, Jianli Li; Project Administration, Jianli Li; Funding Acquisition, Qi qiang Mou.

References

[1] P. Wang, P. Zhang, B. Wang, Y. Zhu, Z. Xu, Z. Zhang, Fatigue cracking criterion of high-strength steels induced by inclusions under high-cycle fatigue, Journal of Materials Science & Technology, 154 (2023) 114.
https://doi.org/ 10.1016/j.jmst.2023.02.006.

[2] J-H. Kang, B. Hosseinkhani, P. E. J. Rivera-Díaz-del-Castillo, Rolling contact fatigue in bearings: multiscale overview, Materials Science and Technology, 28 (2012) 44.
https://doi.org/10.1179/174328413X13758854832157.

[3] C. Gu, M. Wang, Y. Bao, F. Wang, J. Lian, Quantitative analysis of inclusion engineering on the fatigue property improvement of bearing steel, Metals, 9 (2019) 476.
https://doi.org/ 10.3390/met9040476.

[4] H. Wu, Q. Li, C. Wei, C. Wei, Z. Wang, Study on the behaviour of DS-Class inclusions in advanced bearing steel, Metallurgical Research & Technology, 116 (2019) 223. https://doi.org/10.1051/metal/2018096.

[5] N. Liu, G. Cheng, L. Zhang, G. Cheng, L. Zhang, G. Wang. Composition evolution and deformation of different non-metallic inclusions in a bearing steel during hot rolling, Journal of Iron and Steel Research International, 29 (2022) 552. https://doi.org/10.1007/s42243-022-00761-z.

[6] X. Z. Liang, G. H. Zhao, J. Owens, P. Gong, W.M. Rainforth, P.E.J. Rivera-Díaz-del-Castillo, Hydrogen-assisted microcrack formation in bearing steels under rolling contact fatigue, International Journal of Fatigue, 134 (2020) 105485. https://doi.org/10.1016/j.ijfatigue.2020.105485.

[7] N. K. Arakere, Gigacycle rolling contact fatigue of bearing steels: A review, International Journal of Fatigue, 93 (2016) 23. https://doi.org/10.1016/j.ijfatigue.2016.06.034.

[8] C. Gu, W. Liu, J. Lian, Y. Bao, In-depth analysis of the fatigue mechanism induced by inclusions for high-strength bearing steels, International Journal of Minerals, Metallurgy and Materials, 28 (2021) 826. https://doi.org/10.1007/s12613-020-2223-9.

[9] Q. Zeng, W. Hui, Y. Zhang, X. Liu, Z. Yao, Very high-cycle fatigue performance of high carbon-chromium bearing steels with different metallurgical qualities, International Journal of Fatigue, 172 (2023) 107632. https://doi.org/10.1016/j.ijfatigue.2023.107632.

[10] Q. Zeng, J. Li, Q. Xu, Y. Yu, Effect of MgO on crystallization behavior of $MnO–SiO_2–Al_2O_3$ based inclusions in tire cord steel, Heliyon, 8 (2022) 11. https://doi.org/10.1016/j.heliyon.2022.e11800.

[11] Q. Xu, Y. Meng, J. Li, Effect of MgO on structure and crystallization behavior of $CaO–SiO_2–Al_2O_3$ inclusions in Si–Mn deoxidized steel, Journal of Iron and Steel Research International, (2024) 1. https://doi.org/10.1007/s42243-024-01236-z.

[12] C. Wang, X. Liu, J. Gui, Z. Du, Z. Xu, B. Guo. Effect of MnS inclusions on plastic deformation and fracture behavior of the steel matrix at high temperature, Vacuum, 174 (2020) 109209. https://doi.org/10.1016/j.vacuum.2020.109209.

[13] C. Yang, P. Liu, Y. Luan, D. Li, Y. Li, Study on transverse-longitudinal fatigue properties and their effective-inclusion-size mechanism of hot rolled bearing steel with rare earth addition, International Journal of Fatigue, 128 (2019) 105193. https://doi.org/10.1016/j.ijfatigue.2019.105193.

[14] Y. Song, H. Zhang, L. Ren, A review of research on MnS inclusions in high-quality steel, Engineering Reports, 6 (2024) e12892. https://doi.org/10.1002/eng2.12892.

[15] N. Matsuoka, M. Terano, T. Ishiguro, E. Abe, N. Yukawa, T. Ishikawa, Y. Ueshima, K. Yamamoto, K. Isobe, Computer simulation of deformation behavior of non-metallic inclusion in hot-rolling, Procedia Engineering, 81 (2014) 120. https://doi.org/10.1016/j.proeng.2014.09.137.

[16] A. Gupta, S. Goyal, K. A. Padmanabhan, A. K. Singh, Inclusions in steel: micro–macro modelling approach to analyse the effects of inclusions on the properties of steel, The International Journal of Advanced Manufacturing Technology, 77 (2015) 565.
https://doi.org/10.1007/s00170-014-6464-5.

[17] R. Cheng, J. Zhang, B. Wang, Deformation behavior of MnO13%-$Al_2O_3$18%-$SiO_2$69% inclusion in different steels during hot rolling processes, Metallurgical Research & Technology, 114 (2017) 608.
https://doi.org/10.1051/metal/2017058.

[18] H. Zhang, G. Feng, FEM simulation of inclusion in medium plate during rolling, Hot Working Technol, 40 (2011) 41.
https://doi.org/10.1519/JSC.0b013e3181da7858.

[19] J. Ge, Z. Cheng, S. Cheng, Y. Zheng. J. Li. M. Zhou, Evolution of voids around inclusions during CSP hot rolling process, Journal of Iron and Steel Research, 27 (2015) 24.
https://doi.org/10.13228/j.boyuan.issn1001-0963.20130370.

[20] S. Guo, H. Zhu, J. Zhou, M. Song, S. Dong, An in situ scanning electron microscope study of void formation induced by typical inclusions in low-density steel during tensile deformation, Steel Research International, 93 (2022) 2200388.
https://doi.org/10.1002/srin.202200388.

[21] K. Chung, R. Wagoner, Numerical improvement of viscoplastic, non-linear, finite-element analysis, International Journal of Mechanical Sciences, 29 (1987) 45.
https://doi.org/10.1016/0020-7403(87)90073-7.

[22] M. Ahmed, G. Sekhon, D. Singh, Finite element simulation of sheet metal forming processes, Defence Science Journal, 55 (2005) 389.
https://doi.org/10.14429/dsj.55.2002.

[23] R. Cheng, J. Zhang, B. Wang, Deformation behavior of inclusion system CaO–Al_2O_3–SiO_2 with different compositions during hot rolling processes, Transactions of the Indian Institute of Metals, 71 (2018) 705-713.
https://doi.org/10.1007/s12666-017-1203-x.

[24] G. Pan, Z. Luo, C. Lin, Flow stress constitutive equation of as-cast gcr15simn bearing steel, Materials For Mechanical Engineering, 43 (2019) 66-70.
https://doi.org/10.11973/jxgccl201910013.

[25] W. Guo, X. Zheng, Z. Xue, W. Lun, R. Zhou, The simulation analysis of the residual stress which product in the cooling process of sintering alumina ceramic plate by computer, Jiangsu Ceramics, 49 (2016) 20-23.
https://doi.org/10.16860/j.cnki.32-1251/tq.2016.05.007.

[26] J. Miao, L. Yu, X. Liu, B. Guo, High temperature stress–strain curves of MnS and their applications in finite element simulation, Transactions of Nonferrous Metals Society of China, 28 (2018) 2082-2093.
https://doi.org/10.1016/s1003-6326(18)64852-6.

[27] C. Luo, U. Ståhlberg, An alternative way for evaluating the deformation of MnS inclusions in hot rolling of steel, Scandinavian Journal of Metallurgy, 31 (2002) 184-190.
https://doi.org/10.1034/j.1600-0692.2002.310304.x.

[28] Y. Xia, D. Fan, S. Wang, J. Li, Y. He, Effect of isothermal-rolling process on the morphology, size and distribution of Type II MnS, Applied Mechanics and Materials, 364 (2013) 589-593.
https://doi.org/10.4028/www.scientific.net/amm.364.589.

[29] H. Yu, X. Liu, H. Bi, L. Chen, Deformation behavior of inclusions in stainless steel strips during multi-pass cold rolling, Journal of Materials Processing Technology, 209 (2009) 455-461. https://doi.org/10.1016/j.jmatprotec.2008.02.016.

[30] Y. Han, L. Hao, J. Wang, W. Ke, Effect of rare earth addition on corrosion sensitivity of GCr15 bearing steel in marine environment, Materials Letters, 333 (2023) 133693. https://doi.org/10.1016/j.matlet.2022.133693.

[31] Z. Dong, D. Qian, F. Wang, F. Yin, Enhanced impact toughness of previously cold rolled high-carbon chromium bearing steel with rare earth addition, Journal of Materials Engineering and Performance, 30 (2021) 8178-8187. https://doi.org/10.1007/s11665-021-06038-y.

[32] C. Yang, Y. Luan, D. Li, Y. Li. Effects of rare earth elements on inclusions and impact toughness of high-carbon chromium bearing steel, Journal of Materials Science & Technology, 35 (2019) 1298-1308. https://doi.org/10.1016/j.jmst.2019.01.015.

[33] J. M. Summers, S. Chakraborty, L. N. Bartlett, R. J. O'Malley, M. F. Buchely, R. Pilon, On the effect of hot rolling on inclusion size and distribution in a cast AISI 1070 steel railroad wheel, International Journal of Metalcasting, 17(2023) 1277-1295. https://doi.org/10.1007/s40962-022-00854-1

[34] G. Luo, Y. Sui, P. Liu, L. Liang, L. Xu, Effect of La-Ce rare earth on inclusions and impact properties of Q345D steel, Special Steel, 45 (2024) 33. https://doi.org/ 10.20057/j.1003-8620.2023-00253

[35] H. Wang, Y. Bao, J. Zhi, C. Duan, S. Gao, M. Wang, Effect of rare earth Ce on the morphology and distribution of Al2O3 inclusions in high strength IF steel containing phosphorus during continuous casting and rolling process, ISIJ International, 61 (2021) 657-666. https://doi.org/10.2355/isijinternational.isijint-2020-053

Table Contents

Table 1. *Rolling parameters*

Roll diameter(mm)	150
Rolling speed (mm/sec)	942
Slab length L(mm)	200
Slab width H(mm)	100
Inclusion position	(1/2 L, 1/2H)
Inclusion shape	Circle, Ellipse, Square
Rolling temperature (℃)	1100
Reduction(mm）	10
Degree of reduction (%)	10

Table 2. *Chemical composition of GCr15 bearing steel*

Element	**Fe**	**C**	**Si**	**Mn**	**Cr**

Content /*wt.*%	Margin	0.95~1.05	0.40~0.65	0.90~1.20	1.35~1.65
Element	**P**	**S**	**Cu**	**Ni**	**Cu+Ni**
Content /*wt.*%	≤0.027	≤0.020	≤0.25	≤0.30	≤0.50

Table 3. *Flow stress (ε=1 s^{-1})*

Temperature (℃)	950	1000	1050	1100
Flow stress (MPa)				
GCr15	150.3	125.7	104.6	86.9
Al_2O_3	300	250	200	160
MnS	50	45	38	28

Table 4. *Physical parameters*

	GCr15	Al_2O_3	MnS
Density /g· cm^{-3}	7.810	3.95	4.057
Young's modulus /MPa	1.96×10^{11}	3×10^{11}	1.38×10^{11}
Poisson ratio	0.3	0.3	0.3

Figure Contents

(d) 6 μm; (e) 8 μm; (f) 10 μm

Fig. 8. Strain distribution of Al_2O_3-MnS composite inclusions with different sizes Composite inclusion size: round Al_2O_3: (a) 6 μm; (b) 8 μm; (c) 10 μm; Square Al_2O_3: (d) 6 μm; (e) 8 μm; (f) 10 μm

Fig. 9. The stress distribution of different kinds of 6 μm inclusions:(a)circular Al_2O_3; (b) Square Al_2O_3; (c) Circular MnS; (d) Elliptic MnS;(e) Circular Al_2O_3 in circular Al_2O_3-MnS; (f) Square Al_2O_3 in circular Al_2O_3-MnS

Fig. 10. Aspect ratio of MnS inclusions with different sizes and shapes after rolling

Fig. 11. Maximum stress of Al_2O_3 inclusions with different sizes and shapes

Fig. 12. Strain difference at different positions of Al_2O_3 inclusions with different sizes and shapes

Fig. 13. Maximum stress of Al_2O_3-MnS composite inclusions with different sizes after rolling

Fig. 14. Aspect ratio of Al_2O_3-MnS composite inclusions with different sizes after rolling

Fig. 15. The maximum stress of steel matrix around different inclusions with different sizes

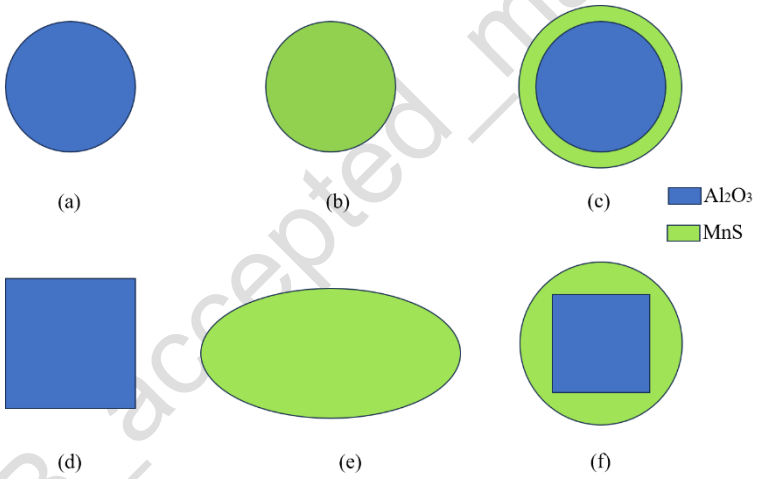

Fig. 1. *Two-dimensional model of different inclusions:(a) circular Al_2O_3;(b) Circular MnS;*

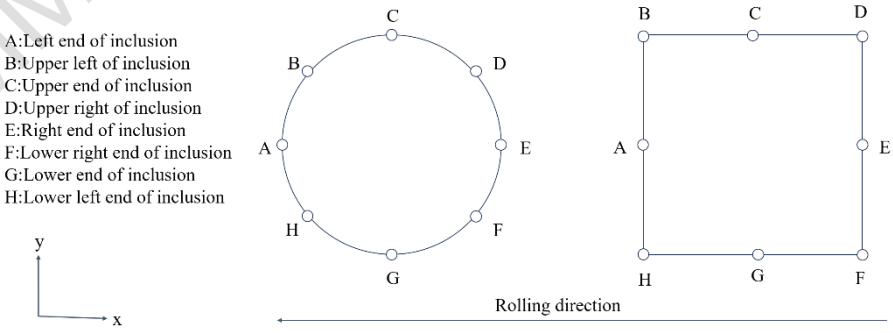

Fig. 2. *Two-dimensional schematic diagram of inclusions*

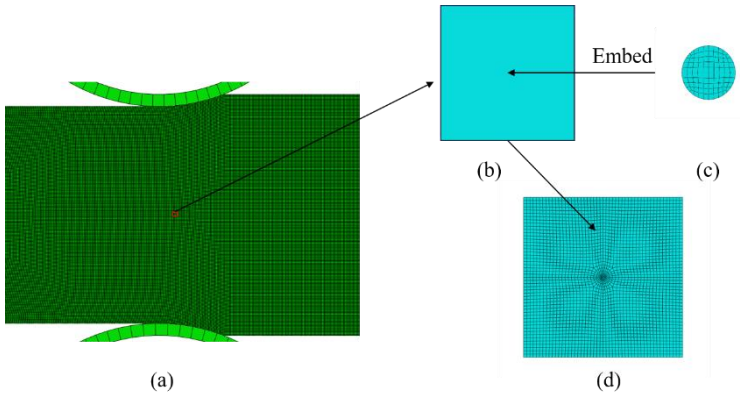

Fig. 3. *Submodel method: (a) Rolling model; (b) Splitting the grid; (c) Inclusions; (d) Submodel*

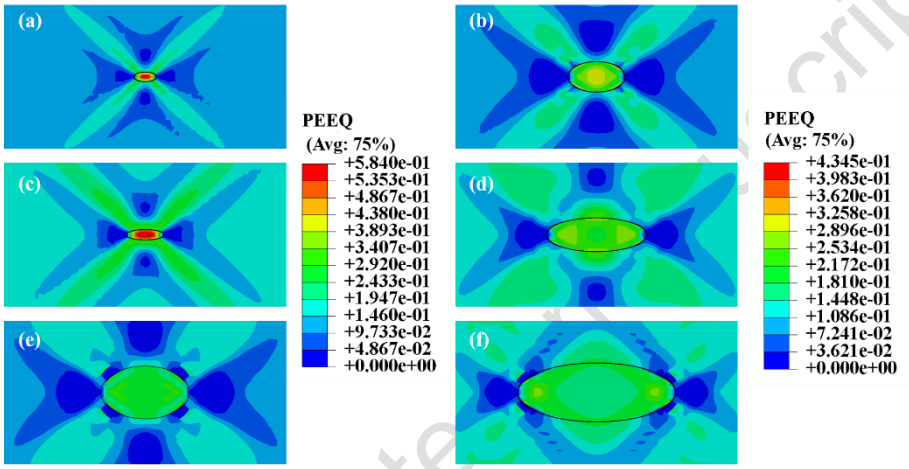

Fig. 4. *Strain distribution of circular and elliptical MnS inclusions with different sizes*
Diameter of round MnS: (a) 2 μm; (c) 6 μm; (e) 10 μm;
Elliptical MnS minor axis length: (b) 2 μm; (d) 6 μm; (f)10 μm

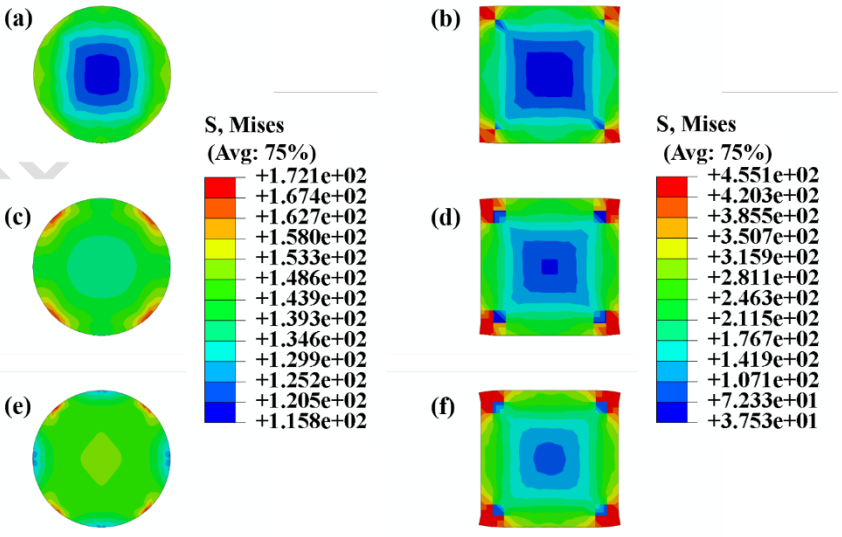

Fig. 5. *The stress distribution of Al_2O_3 inclusions with different sizes and shapes:*
Circular diameter: (a) 2 μm; (b) 6 μm; (c) 10 μm; Square side length: (d) 2 μm; (e) 6 μm; (f) 10 μm

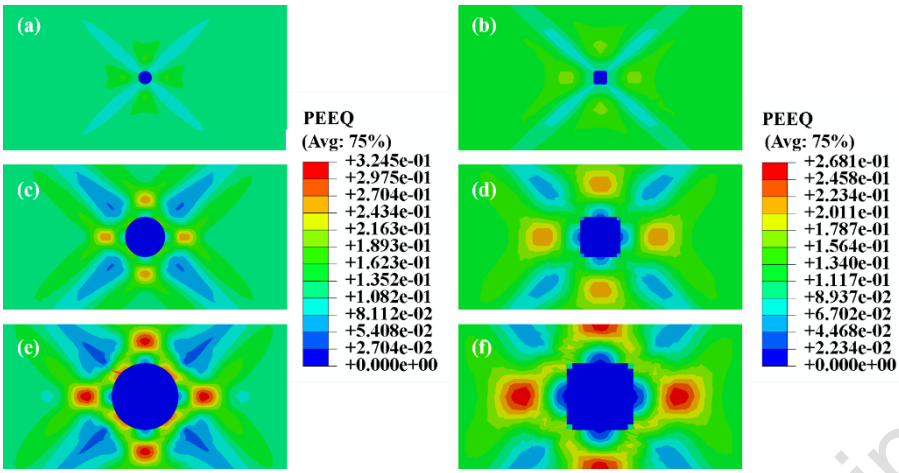

Fig. 6. *Strain distribution of Al_2O_3 inclusions with different sizes: Circular diameter: (a) 2 μm; (b) 6 μm; (c) 10 μm; Square side length: (d) 2 μm; (e) 6 μm; (f) 10 μm*

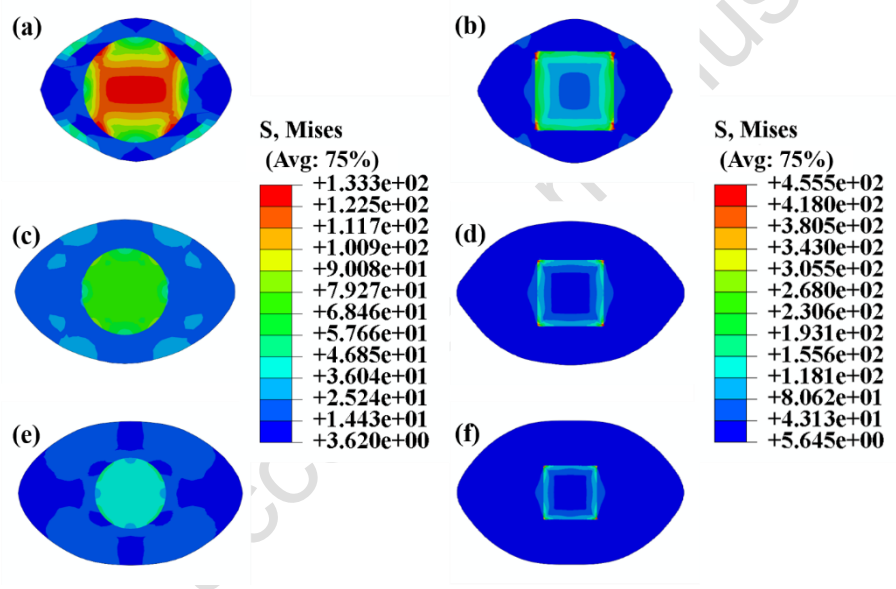

Fig. 7. *Stress distribution of Al_2O_3-MnS inclusions with different sizes and shapes Composite inclusion size: round Al_2O_3: (a) 6 μm; (b) 8 μm; (c) 10 μm; Square Al_2O_3: (d) 6 μm; (e) 8 μm; (f) 10 μm*

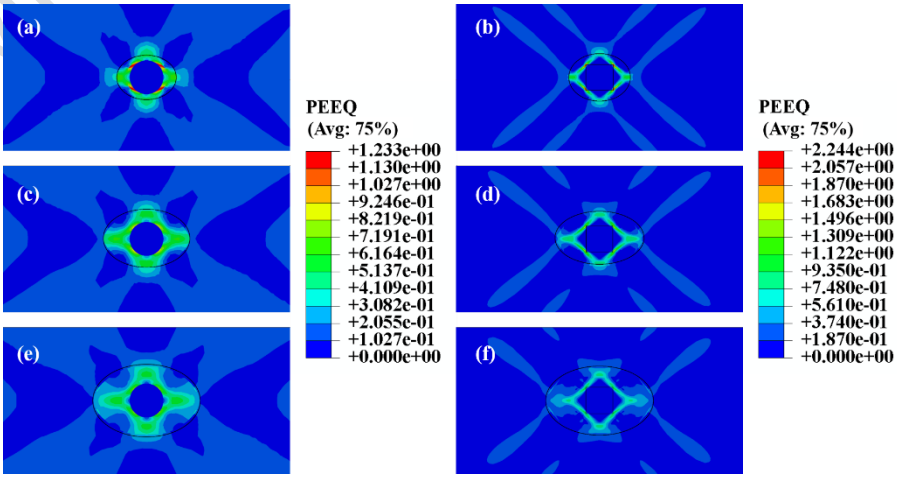

Fig. 8. *Strain distribution of Al_2O_3-MnS composite inclusions with different sizes*
Composite inclusion size: round Al_2O_3:
(a) 6 μm; (b) 8 μm; (c) 10 μm; Square Al_2O_3: (d) 6 μm; (e) 8 μm; (f) 10 μm

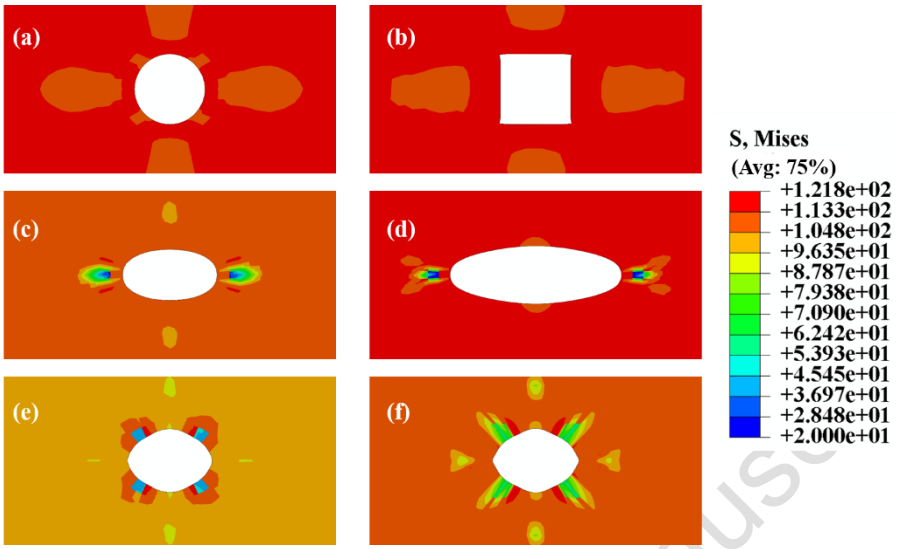

Fig. 9. *The stress distribution of different kinds of 6 μm inclusions:*
(a)circular Al_2O_3; (b) Square Al_2O_3; (c) Circular MnS; (d) Elliptic MnS;
(e) Circular Al_2O_3 in circular Al_2O_3-MnS; (f) Square Al_2O_3 in circular Al_2O_3-MnS

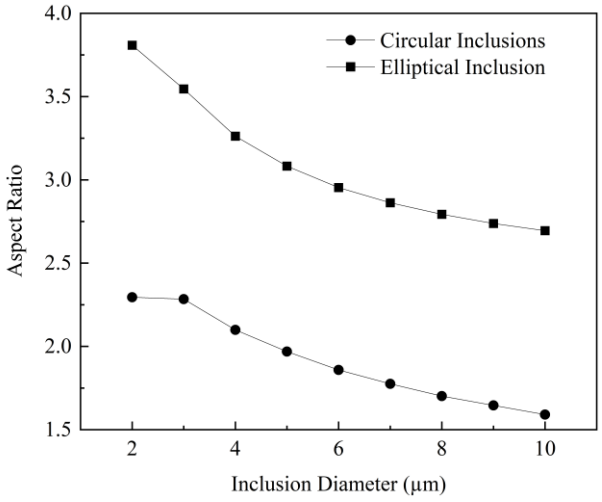

Fig. 10. *Aspect ratio of MnS inclusions with different sizes and shapes after rolling*

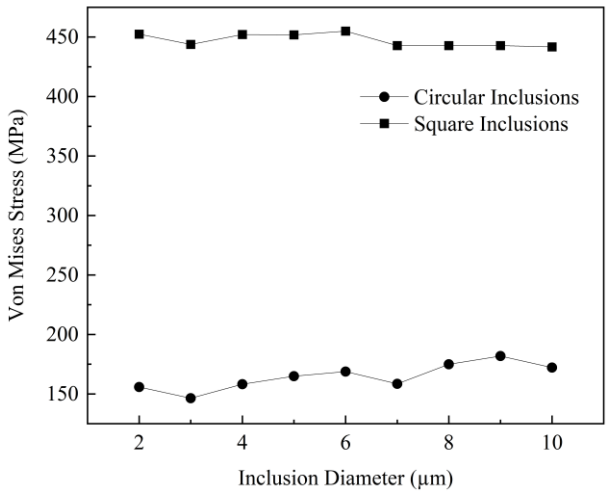

Fig. 11. *Maximum stress of Al_2O_3 inclusions with different sizes and shapes*

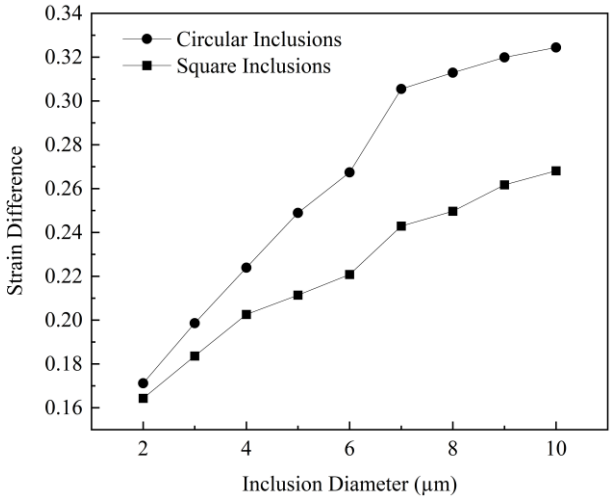

Fig. 12. *Strain difference at different positions of Al_2O_3 inclusions with different sizes and shapes*

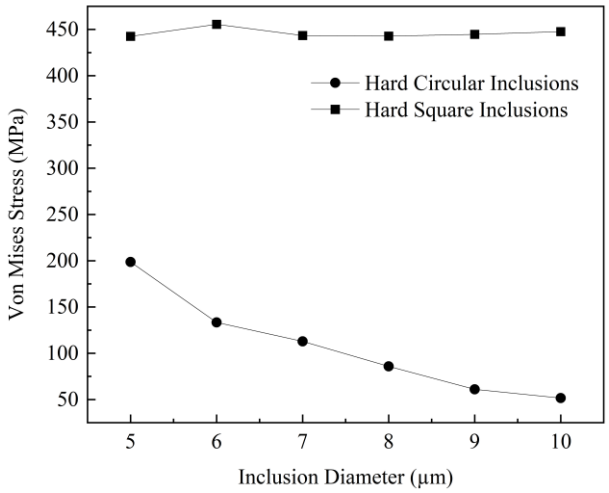

Fig. 13. *Maximum stress of Al_2O_3-MnS composite inclusions with different sizes after rolling*

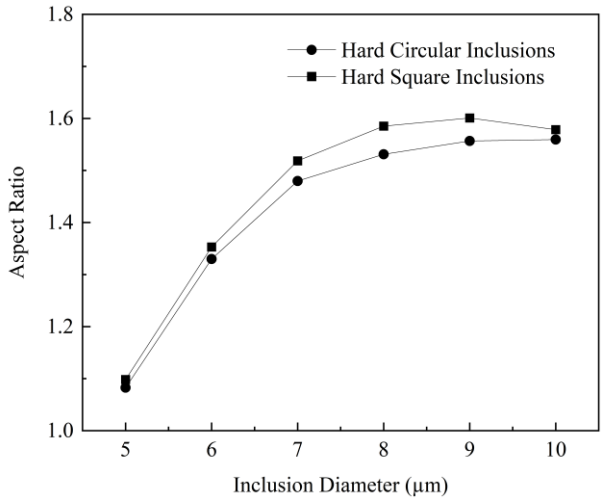

Fig. 14. *Aspect ratio of Al_2O_3-MnS composite inclusions with different sizes after rolling*

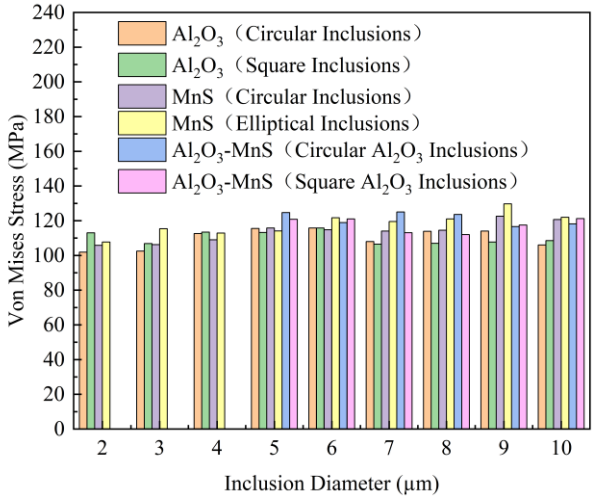

Fig. 15. The maximum stress of steel matrix around different inclusions with different sizes